



# Hetero-phase Pd<sub>4</sub>S metallene nanoribbons with Pd-rich vacancies for sulfur ion degradation-assisted hydrogen production

Wenxin Wang, Qiqi Mao, Shaojian Jiang, Kai Deng, Hongjie Yu, Ziqiang Wang, You Xu, Liang Wang, Hongjing Wang\*

State Key Laboratory Breeding Base of Green-Chemical Synthesis Technology, College of Chemical Engineering, Zhejiang University of Technology, Hangzhou 310014, PR China

## ARTICLE INFO

### Keywords:

Metallene  
Nanoribbon  
Pd<sub>4</sub>S  
Pd vacancies  
Water splitting

## ABSTRACT

Vacancy defects and crystal-phase are essential parameters that affect surface electronic structure. It is still a great challenge to introduce both vacancy defects and unconventional crystal-phase into electrocatalysts to investigate their effects on the electrocatalytic performance. Herein, we in-situ constructed ultrathin Pd<sub>4</sub>S metallene nanoribbon with Pd-rich vacancies (V<sub>Pd</sub>-Pd<sub>4</sub>S MNRs) via hydrothermal sulfuration for outstanding hydrogen evolution reaction (HER) and sulfion oxidation reaction (SOR) performance. Based on the metallene morphology, synergistic effect of Pd vacancies and crystal-phase, V<sub>Pd</sub>-Pd<sub>4</sub>S MNRs exhibits excellent activity and long-term stability, reaching 100 mA cm<sup>-2</sup> at 0.776 V to accomplish the simultaneous hydrogen production and sulfur ion degradation. As confirmed by density functional theory (DFT) simulations, the vacancies and S atoms affect electronic structure of catalyst surface, modulating the *d*-band center of Pd and thus optimizing the adsorption/dissociation during catalytic process. This work presents a promising method to simultaneously construct metal vacancies and crystal-phase in metallene electrocatalysts.

## 1. Introduction

Hydrogen (H<sub>2</sub>), which is used to produce high energy density, clean and abundant reserves, is widely considered as a promising alternative to fossil resources as a sustainable energy source that can alleviate the rapidly growing energy demand [1–7]. Among the various technologies for H<sub>2</sub> production, electrocatalytic overall water splitting (OWS) via two half-reactions: cathodic HER and anodic oxygen evolution reaction (OER), is currently recognized as a simple and environmentally friendly way to produce H<sub>2</sub> [8–12]. However, the anode OER with slow kinetics directly leads to high drive voltage (typically ≥1.8 V) and low H<sub>2</sub> production efficiency, which seriously hinders the practical application of OWS [13–15]. Industrial sewage enriched with sulfur ions has been seriously damaging the ecological environment. SOR (S<sup>2-</sup> → S↓ + 2e<sup>-</sup>) can recover the sulfur source without adding additional oxidants, which is important for environmental restoration [16,17]. Moreover, SOR is intriguing due to its inherently low thermodynamic potential [18–21]. In addition to the low energy consumption for H<sub>2</sub> production, the overall SOR-coupled HER electrolysis (HER+SOR) provides an opportunity for efficient sulfur ion degradation and recovery of sulfur at the anode,

which has practical implications for environmental protection. However, it remains a significant challenge to explore the high-performance bifunctional electrocatalysts for the newly coupled system mentioned above.

With inherent advantages and excellent performance, Palladium (Pd) has been widely used in various cathodic and anodic electrocatalytic reactions in recent years, such as, HER, CO<sub>2</sub> reduction (CO<sub>2</sub>RR), methanol oxidation reaction (MOR), oxygen reduction reaction (ORR), etc [22–24]. Given that the catalytic reaction mainly occurs on the catalyst surfaces, the active sites can be regulated by constructing low-dimensional nanomorphology, which is an effective method to optimize Pd-based electrocatalysts [25]. In terms of morphology, it is considered that metallene as a new type of ultrathin two-dimensional (2D) nanomaterial is currently a promising choice for electrocatalysts in the field of electrocatalysis, which has the advantages of high specific surface area, surface metal atoms with low coordination and good electrical conductivity [26–32]. More importantly, the electronic structure adjustment on the surface of metallene provides an effective strategy for enhancing catalytic performance, including defect-, strain-, phase- and interface engineering [33–35]. Among them, the existence of

\* Corresponding author.

E-mail address: [hjw@zjut.edu.cn](mailto:hjw@zjut.edu.cn) (H. Wang).

<https://doi.org/10.1016/j.apcatb.2023.123194>

Received 31 May 2023; Received in revised form 31 July 2023; Accepted 19 August 2023

Available online 21 August 2023

0926-3373/© 2023 Elsevier B.V. All rights reserved.

metal vacancy defects leads to unsaturated bonding of atoms and serves to optimize the surface electronic structure of the electrocatalyst [19,36,37]. For example, Wang et al. controllably synthesized  $\text{PdH}_x$  metallene with Pd vacancies and the presence of Pd vacancies can promote the adsorption and activation of  $\text{N}_2$  during NRR, thus exhibiting NRR at low potentials [38]. Guo et al. reported that Pd metallene with a large number of atomic-level Pd vacancies showed excellent ORR activity in regulating the adsorption strength of intermediates during the reaction [39]. However, the formation of metal vacancies is still highly energetic and difficult to be controlled [40]. Besides the introduction of vacancies, phase engineering has recently been another important way to regulate the electronic and intrinsic properties of catalysts, especially crystal-phase imparting higher electrical conductivity and electron transport properties [41,42]. For example, Liu et al. reported that unconventional hexagonal closed packed (*hcp*) Pd exhibited even better catalytic activity than Pt in electrocatalytic HER compared with conventional face-centered cubic (*fcc*) Pd [43]. Our group prepared P-doped  $\text{Pd}_4\text{S}$  nanowires with Pt/C-like catalytic activity in HER [44]. Moreover, the formation of crystalline/amorphous regions can endow the catalyst with advantages of abundant active sites and faster electron transport capacity compared to crystalline or amorphous regions [45–48]. Zhong et al. synthesized a crystalline-amorphous  $\text{CoSe}_2/\text{CoP}$  heterojunction that benefits from strong electronic interactions at the crystalline/amorphous interface and can exhibit excellent activity in HER [49]. Nevertheless, most of the current researches have focused on Pd-based materials with conventional crystal-phases. Therefore, it is highly desired to develop an effective and simple method for constructing Pd-based electrocatalysts with metal vacancy and unconventional crystal-phases, simultaneously [50].

Based on the above considerations, we propose a sulfuration method for the in-situ preparation of  $\text{V}_{\text{Pd}}\text{-Pd}_4\text{S}$  MNRs. The strategy achieves the formation of Pd vacancies and transformation of crystal-phase by atomic exchange and leaching of Mo atoms during the  $\text{PdMoO}_x$  metallene nanoribbons ( $\text{PdMoO}_x$  MNRs) sulfuration process. Moreover, the modulation of the surface electronic structure of Pd by vacancies and S atoms, which causes the change of the *d*-band center, is further revealed by DFT. Benefited from this, the  $\text{V}_{\text{Pd}}\text{-Pd}_4\text{S}$  MNRs show superior performance in terms of both HER and SOR processes, and only 0.776 and 0.865 V are required to reach 100 and 200  $\text{mA cm}^{-2}$  in the constructed coupled system for simultaneous low-energy  $\text{H}_2$  production and sulfur ion wastewater degradation.

## 2. Experimental section

### 2.1. Synthesis of $\text{V}_{\text{Pd}}\text{-Pd}_4\text{S}$ MNRs

$\text{PdMoO}_x$  MNRs were synthesized as precursors according to the method reported by our group with minor modifications [51]. L-ascorbic acid (AA) (80 mg), polyvinyl pyrrolidone (PVP) (600 mg,  $M_w = 40,000$ ) and  $\text{Mo}(\text{CO})_6$  (50 mg) were added to a 30 mL glass vial containing ethanediamine (EN) (2 mL) and dissolved by ultrasonication. Then,  $\text{Na}_2\text{PdCl}_4$  (0.5 mL, 0.1 M) was injected into the above mixture solution and dispersed well by sonication. The reaction was carried out in an oil bath at 120 °C for 8 h. The resulting black colloidal products were centrifuged, washed and dried for use. To prepare  $\text{V}_{\text{Pd}}\text{-Pd}_4\text{S}$  MNRs, the obtained  $\text{PdMoO}_x$  MNRs (5 mg) and  $\text{Na}_2\text{S}$  (30 mg) were first mixed and dissolved in  $\text{H}_2\text{O}$  (15 mL) water. The well-mixed black solution was then poured into a 25 mL Teflon-lined stainless steel autoclave and heated at 120 °C for 8 h. The obtained black product was collected by centrifugation and washed for certain times with ethanol/ $\text{H}_2\text{O}$ .

### 2.2. Electrochemical experiments

The as-prepared samples were dispersed in a mixed solution (ultrapure water:ethanol:Nafion (0.5 wt%) = 7:2:1) and sonicated for 30 min to form an ink solution. All electrochemical data were performed at a

CHI660E electrochemical workstation. A three-electrode system (glassy carbon electrode as working electrode, graphite rod as counter electrode and  $\text{Hg}/\text{HgO}$  (1 M KOH) electrode as reference electrode) was used to conduct HER/SOR tests. 5  $\mu\text{L}$  of ink was deposited on the glassy carbon electrode. For the two-electrode system, 5 mg/mL of sample was dropped on  $1 \times 1 \text{ cm}^2$  carbon paper (CP) paper to achieve a loading of 1  $\text{mg cm}^{-2}$ , which was applied to the positive and negative electrodes, respectively. For electrochemical assessments, Linear sweep voltammetry (LSV) polarization curves were recorded in 1 M KOH/1 M KOH + 4 M  $\text{Na}_2\text{S}$  at speed of 5 mV/s with 95% iR-compensation. Chronopotentiometry (*v-t*) test was recorded at 10  $\text{mA cm}^{-2}$  for 20 h. The electrochemical impedance (EIS) curves were carried out in a frequency range from 100 kHz to 0.1 Hz. All potential was converted to reversible hydrogen electrode (RHE) follows the equation:  $E_{\text{RHE}} = E_{\text{Hg}/\text{HgO}} + 0.095 + 0.059 \times \text{pH}$ .

## 3. Results and discussion

### 3.1. Synthesis and characterization of $\text{V}_{\text{Pd}}\text{-Pd}_4\text{S}$ MNRs

The synthesis diagram of  $\text{V}_{\text{Pd}}\text{-Pd}_4\text{S}$  MNRs was demonstrated in Fig. 1. The  $\text{PdMoO}_x$  MNRs with highly curled features (Fig. S1) were prepared in the presence of the structure directing agents of  $\text{Mo}(\text{CO})_6$  and PVP, and reducing agent of AA. Then, the obtained  $\text{PdMoO}_x$  MNRs were used as precursors for sulfuration to prepare  $\text{V}_{\text{Pd}}\text{-Pd}_4\text{S}$  MNRs. As shown in high angle annular dark field scanning transmission electron microscopy (HAADF-STEM) and transmission electron microscopy (TEM) images, the  $\text{V}_{\text{Pd}}\text{-Pd}_4\text{S}$  MNRs possessed a coiled and folded 2D nanoribbon structure with a width of about 20 nm, indicating that the overall morphology is maintained during the sulfuration process (Fig. 2a and 2b). It was further observed by high magnification TEM that the nanoribbons are composed of metallene stacked on top of each other (Figs. 2c–2e). The large number of metallene dislocated and self-assembled to form vein structure provides sufficient channels for mass transfer to promote catalytic performance [52,53]. Moreover, the thickness of  $\text{V}_{\text{Pd}}\text{-Pd}_4\text{S}$  MNRs is about 1.1 nm characterized by atomic force microscopy (AFM), demonstrating their ultrathin graphene-like properties (Fig. 2f). High-resolution TEM (HRTEM) images were further carried out to characterize the atomic structure of  $\text{V}_{\text{Pd}}\text{-Pd}_4\text{S}$  MNRs. It can be seen that partial amorphous regions have been formed due to the disorganization of the atomic arrangements triggered by the introduction of larger radius S atoms, resulting in the conversion of a part of the crystalline region into an amorphous region (Fig. 2g) [54]. In addition, the (I) and (II) regions of Fig. 2g is enlarged and it is found that the 0.25 and 0.23 nm lattice stripes correspond to the (200) and (210) crystal planes of tetragonal  $\text{Pd}_4\text{S}$ , respectively [44,55–57]. Apart from that, the continuous diffraction rings of  $\text{V}_{\text{Pd}}\text{-Pd}_4\text{S}$  MNRs were observed by the selected area electron diffraction (SAED), reflecting its polycrystalline nature (the inset of Fig. 2g). Meanwhile, the Pd vacancies of  $\text{V}_{\text{Pd}}\text{-Pd}_4\text{S}$  MNRs can be observed in the white dashed circle (Fig. 2h) and the atomic models are shown in Fig. 2i. The Pd vacancies were also confirmed by electron paramagnetic resonance (EPR) characterization (Fig. 2j). The signal of  $\text{V}_{\text{Pd}}\text{-Pd}_4\text{S}$  MNRs near 2816 G is significantly enhanced compared to  $\text{PdMoO}_x$  MNRs, indicating that the capture of electrons by Pd vacancies on the  $\text{V}_{\text{Pd}}\text{-Pd}_4\text{S}$  MNRs surface [39]. The

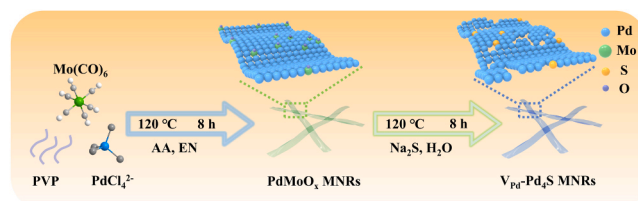
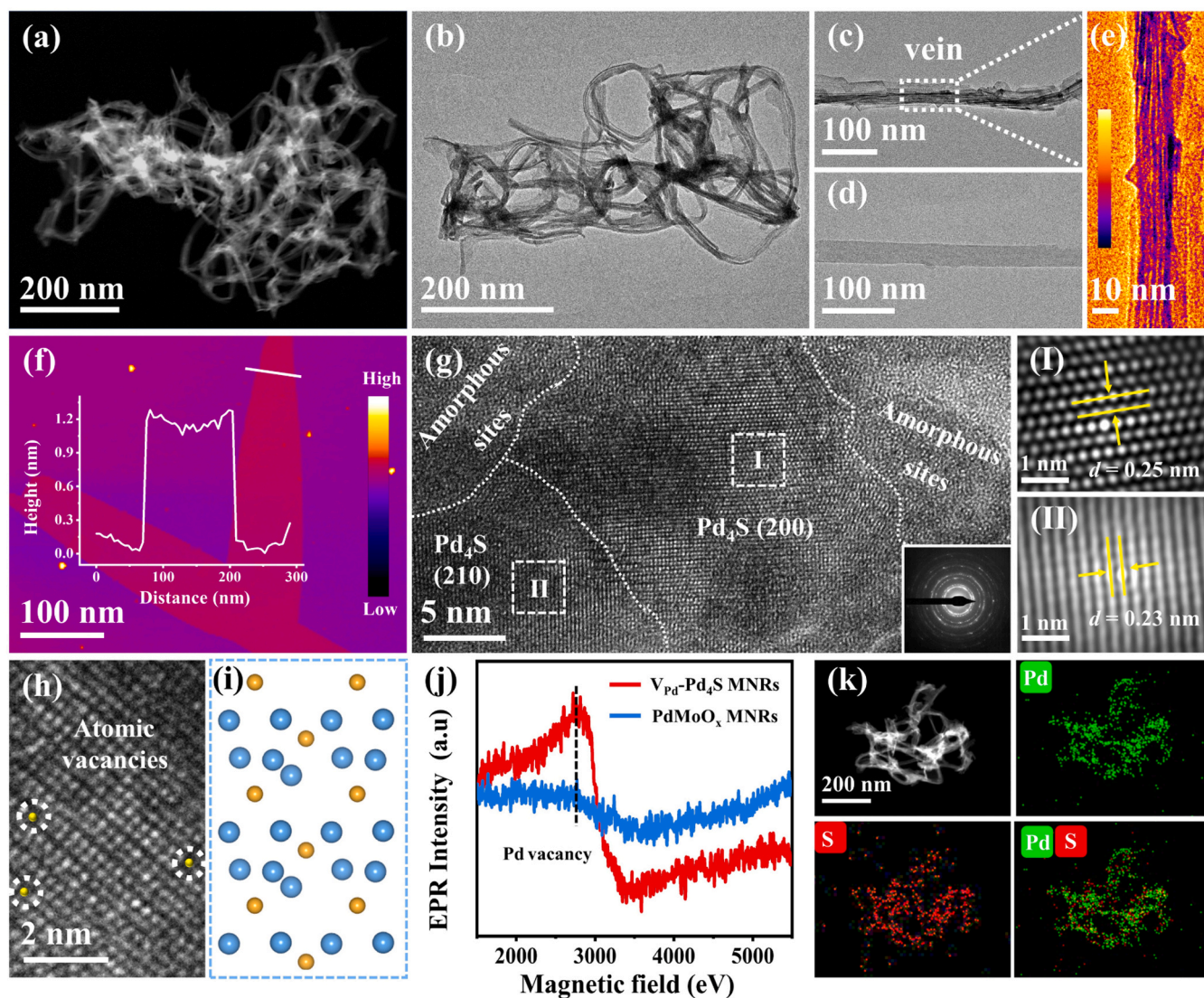


Fig. 1. Schematic representation of the synthesis of  $\text{V}_{\text{Pd}}\text{-Pd}_4\text{S}$  MNRs.





**Fig. 2.** Morphological and structure characterizations of  $V_{Pd}$ -Pd<sub>4</sub>S MNRs. (a) HAADF-STEM, (b, c and d) TEM, (e) False-color high-magnification TEM and (f) AFM images of the  $V_{Pd}$ -Pd<sub>4</sub>S MNRs. (g) HRTEM image of  $V_{Pd}$ -Pd<sub>4</sub>S MNRs and the corresponding lattice fringes patterns in the specified locations in (I) and (II). (h) HRTEM image of  $V_{Pd}$ -Pd<sub>4</sub>S MNRs and (i) the corresponding atomic models of Pd<sub>4</sub>S. (j) EPR spectra of  $V_{Pd}$ -Pd<sub>4</sub>S MNRs and PdMoO<sub>x</sub> MNRs. (k) HAADF-STEM and the corresponding EDX mapping images of the  $V_{Pd}$ -Pd<sub>4</sub>S MNRs.

sulfuration process induces not only the generation of amorphous/crystalline hetero-phase structures and crystal-phase of tetragonal Pd<sub>4</sub>S, but also the formation of Pd vacancies. The structural evolution of  $V_{Pd}$ -Pd<sub>4</sub>S MNRs may affect the coordination environment and number of the active site on the surface, leading to large changes in the electronic structure and thus improving the electrocatalytic performance [38,58]. The HAADF-STEM and the corresponding elemental mapping images show that Pd and S were uniformly existed throughout the nanoribbon (Fig. 2k), which the corresponding TEM- energy dispersive X-ray spectroscopy (EDX) spectrum shows Pd/S atomic ratio  $\approx 1.9/1$  (Fig. S2). The result is essentially similar to that of inductively coupled plasma optical emission spectrometry (ICP-OES) (Pd/S  $\approx 2.0/1$ ).

X-ray diffractometer (XRD) tests were employed to investigate the crystal structures of  $V_{Pd}$ -Pd<sub>4</sub>S MNRs and PdMoO<sub>x</sub> MNRs. As shown in Fig. 3a, the peak positions of PdMoO<sub>x</sub> MNRs basically correspond to the reference standard card for Pd (JCPDS:46–1043), indicating a typical *fcc* phase structure. However, all diffraction peaks of  $V_{Pd}$ -Pd<sub>4</sub>S MNRs are well directed with tetragonal Pd<sub>4</sub>S (JCPDS:10–0335). The diffraction peaks of  $V_{Pd}$ -Pd<sub>4</sub>S MNRs are found to be slightly shifted to a small angle by zooming in the  $30^\circ - 45^\circ$  region, which may be due to the presence of

vacancies [59]. The in-situ XRD results show that the *fcc* phase of PdMoO<sub>x</sub> MNRs gradually transforms into tetragonal Pd<sub>4</sub>S of  $V_{Pd}$ -Pd<sub>4</sub>S MNRs during the sulfuration process. The elemental composition and valence states of the samples were analyzed by X-ray photoelectron spectroscopy (XPS) measurements. The comparison of the full-scan XPS survey spectrum clearly revealed that the Mo element is absent in  $V_{Pd}$ -Pd<sub>4</sub>S MNRs compared to PdMoO<sub>x</sub> MNRs (Fig. 3b). The high-resolution XPS spectra of Pd 3d can be convoluted into 3d<sub>2/3</sub> and 3d<sub>5/2</sub> (Fig. 3c). In the case of PdMoO<sub>x</sub> MNRs, the binding energies of 340.0 and 334.8 eV are attributed to the Pd<sup>0</sup>, while 341.3 and 335.7 eV correspond to Pd<sup>2+</sup>. It can be clearly observed that the Pd 3d orbitals of  $V_{Pd}$ -Pd<sub>4</sub>S MNRs show a positive shift of approximately 0.76 eV compared to PdMoO<sub>x</sub> MNRs. The possible reasons for the movement of  $V_{Pd}$ -Pd<sub>4</sub>S MNRs to higher binding energies might be ascribed to the presence of vacancies during sulfuration or the transfer of electrons from Pd atom to S atom [60,61]. Fig. 3d displays that for the Mo 3d binding energy of PdMoO<sub>x</sub> MNRs one set of peaks is located at 235.4 and 234.7 eV, while the other peaks are located at 232.5 and 232.0 eV corresponding to the Mo 3d<sub>3/2</sub> and 3d<sub>5/2</sub> orbitals, respectively, which sufficiently indicates that the Mo element is exclusively present in the

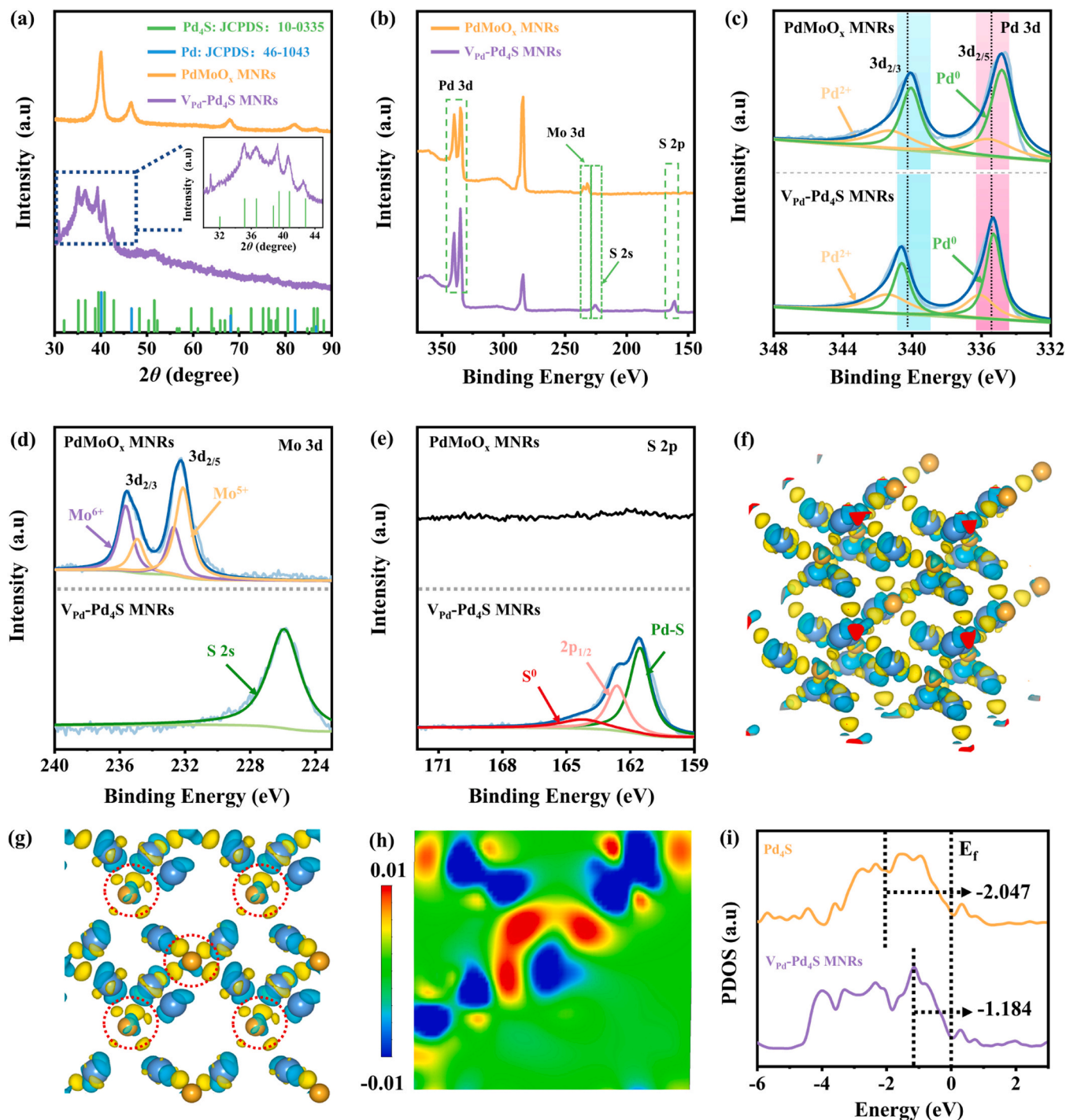


**Fig. 3.** (a) XRD patterns of  $V_{Pd}$ - $Pd_4S$  MNRs and  $PdMoO_x$  MNRs. The inset in (a) is the corresponding zoom-in regions between  $2\theta$  at  $30^\circ$  and  $45^\circ$ . (b) XPS survey spectrum of  $V_{Pd}$ - $Pd_4S$  MNR. High-resolution XPS spectra: (c) Pd 3d, (d) Mo 3d and (e) S 2p for  $V_{Pd}$ - $Pd_4S$  MNRs and  $PdMoO_x$  MNRs. (f) and (g) Charge density difference of the  $V_{Pd}$ - $Pd_4S$  MNRs model (yellow and blue regions indicate the electron accumulation and deletion, respectively). (h) Charge density difference of  $V_{Pd}$ - $Pd_4S$  MNRs bulk structure. The electron delocalizing trend is from  $-0.01$ – $0.01$ . (i) The PDOS for  $V_{Pd}$ - $Pd_4S$  MNRs bulk and  $Pd_4S$  bulk.

oxidation state. In a contrast, the broad peak of  $V_{Pd}$ - $Pd_4S$  MNRs at 225.9 eV is attributed to the S 2s orbital, while the Mo element is not detected in the Mo 3d orbital of  $V_{Pd}$ - $Pd_4S$  MNRs [55]. Notably, the main peaks 162–164 eV in the S 2p orbitals of  $V_{Pd}$ - $Pd_4S$  MNRs are belonged to the “alloy type compound”  $Pd_4S$  rather than the sulfide [57,62]. Specifically, the two peaks with binding energies of 162.6 and 161.5 eV are associated with  $2p_{1/2}$  and  $2p_{3/2}$  orbitals of  $S^{2-}$ , respectively, directly indicating the formation of Pd-S bonds (Fig. 3e) [19,44,63]. Meanwhile, the O 1s orbitals of  $V_{Pd}$ - $Pd_4S$  MNRs and  $PdMoO_x$  MNRs reveal the

presence of two different O states, lattice oxygen ( $O_{OL}$ ) and metal-oxygen bonds ( $O_{MO-O}$ ), respectively. From Fig. S3, it can be observed that the peaks of  $O_{OL}$  for  $V_{Pd}$ - $Pd_4S$  MNRs get larger while the peaks of  $O_{MO-O}$  get smaller, indicating a large number of defect sites and a reduction of Mo-O bonds, respectively [64,65]. To reveal the influence of the corresponding regulatory electronic states and vacancies of the  $V_{Pd}$ - $Pd_4S$  MNRs on the d-band center, DFT simulations were executed. The charge density difference plots are exploited to reveal the electron transfer of  $V_{Pd}$ - $Pd_4S$  MNRs. As shown in Figs. 3f–3h, the electrons



accumulate near the S atom and dissipate around the Pd atom. The further calculation of electron gain and loss around specific  $V_{Pd}$ -Pd<sub>4</sub>S MNRs atoms by Bader charge reveals that the Pd atom loses 0.15 e and the S atom gains 0.15 e of total net charge (Fig. S4). The result proves that the process of electrons from Pd to S is consistent with the above XPS analysis. By calculating the projected partial density of states (PDOS) of  $V_{Pd}$ -Pd<sub>4</sub>S MNRs and Pd<sub>4</sub>S without vacancies, it is shown that the center of the *d*-band of the former (−1.184 eV) is significantly shifted upward compared to the latter (−2.047 eV) (Fig. 3i). This phenomenon is attributed to the presence of Pd vacancies regulating the surface electronic structure of Pd, which leads to the alteration of the *d*-band center [66,67]. The change of *d*-band can optimize the adsorption/dissociation of reactants/intermediates in the electrocatalytic process and serve to improve the electrocatalytic activity [68–70].

### 3.2. Analysis of Pd vacancies formation in $V_{Pd}$ -Pd<sub>4</sub>S MNRs

In order to elucidate the process of vacancies formation and structural transformation during sulfuration, we depicted the sulfuration schematic (Fig. 4a) and characterized the samples with different sulfuration times by TEM, EDS and XRD. It was observed from the TEM images that the morphology of the nanoribbons of the samples remained constant throughout the sulfuration process (Figs. 4b–4d). The atomic ratio of Pd:Mo for PdMoO<sub>x</sub> MNRs is 92.81: 7.19. After 4 h of sulfuration, the atomic ratio of Pd:Mo:S changed to 64.77: 0.73: 34.50, and the content of Mo atoms decreased rapidly. When the sulfuration time is extended to 8 h, the atomic ratio of Pd:Mo:S was 64.97: 0: 35.03, indicating that the Mo atoms were completely leach out (Fig. 4e). It can be observed that Pd gradually transforms from the *fcc* structure to the tetragonal Pd<sub>4</sub>S with the extension of time (Fig. S5). Moreover, different contents of Na<sub>2</sub>S were used for sulfuration to investigate the effect of the content on its structure. From the XRD images, it can be analyzed that the increase of Na<sub>2</sub>S content did not change the structure of the tetragonal Pd<sub>4</sub>S (Fig. S6). Based on the characteristics of the sulfuration process, we suggest that it may be the substitution of O atoms in the host crystal PdMoO<sub>x</sub> MNRs by heterogeneous S atoms leads to the breakage of Mo–O bonds thus causing the loss of Mo atoms, resulting in the

formation of Pd vacancies. At the same time, Pd atoms are coordinated to S atoms to form bonds and the structure is transformed from *fcc* of Pd to tetragonal Pd<sub>4</sub>S, while the difference in electronegativity and atomic radius of S and O atoms leads to the destruction of the original crystal structure and the formation of amorphous regions. Apart from, the effect of sulfuration temperature on the crystal phase of the samples was also explored. XRD pattern show that the crystal phase of Pd gradually changes from *fcc* to tetragonal Pd<sub>4</sub>S with the increase of temperature. However, the sample transforms to Pd<sub>2</sub>S at 200 °C, which indicates that the change of temperature affects the content of S and thus the crystal-phase of the sample (Fig. S7).

### 3.3. HER and SOR electroactivity of $V_{Pd}$ -Pd<sub>4</sub>S MNRs

To test the HER catalytic activity of various catalysts, the experiments were conducted in 1 M KOH electrolyte by a typical three-electrode system. Fig. 5a shows the HER polarization curves of all samples, with PdMoO<sub>x</sub> MNRs and Pd black as the comparison. The HER activity of  $V_{Pd}$ -Pd<sub>4</sub>S MNRs clearly far exceeds that of Pd black, while it has a higher activity compared to PdMoO<sub>x</sub> MNRs. The corresponding Tafel slope of  $V_{Pd}$ -Pd<sub>4</sub>S MNRs is 43.3 mV dec<sup>−1</sup> similarly smaller than that of PdMoO<sub>x</sub> MNRs (109.2 mV dec<sup>−1</sup>) and Pd black (242.2 mV dec<sup>−1</sup>), implying a more favorable reaction kinetics (Fig. 5b). The Tafel slope of  $V_{Pd}$ -Pd<sub>4</sub>S MNRs follows a Volmer-Heyrovsky mechanism, in which chemical desorption is the rate-determining step [71]. The Pd vacancies modulate the local electronic structure of the surface to accelerate the active H adsorption, thus enhancing the catalytic activity of HER [44]. By comparison, it was found that the HER activity of  $V_{Pd}$ -Pd<sub>4</sub>S MNRs also exceeds that of some other Pd-based electrocatalysts reported in the literature (Table S1). Obviously, the EIS were investigated during HER process (Fig. S8). The  $V_{Pd}$ -Pd<sub>4</sub>S MNRs on the catalytic electrode surface exhibited the smallest semicircular diameter, where the semicircular diameter is proportional to the charge transfer resistance. These reasons can be attributed to the fact that the partially amorphous region and the nanoribbon comprising the network structure of  $V_{Pd}$ -Pd<sub>4</sub>S MNRs facilitates the charge transfer between the catalyst surface and the electrolyte. Except for HER evaluated for the cathode, the  $V_{Pd}$ -Pd<sub>4</sub>S MNRs has also received focus as an anode SOR material. To test the effect of Na<sub>2</sub>S addition on HER, the HER polarization curves of  $V_{Pd}$ -Pd<sub>4</sub>S MNRs were tested in 1 M KOH + 4 M Na<sub>2</sub>S solution. The polarization curves are found to be almost invariant in the presence or absence of Na<sub>2</sub>S, indicating that the effect of Na<sub>2</sub>S in 1 M KOH on the catalyst HER performance is negligible (Fig. 5c). The LSV curves for different Na<sub>2</sub>S concentrations were presented in Fig. S9, and it is clearly found that  $V_{Pd}$ -Pd<sub>4</sub>S MNRs has the optimum catalytic activity in 4 M Na<sub>2</sub>S. As shown in Fig. 5d, the  $V_{Pd}$ -Pd<sub>4</sub>S MNRs also exhibits better SOR activity and the advantage is more pronounced with increasing current density. The Tafel slope plot similarly reveals that  $V_{Pd}$ -Pd<sub>4</sub>S MNRs has a smaller slope at the SOR process (Fig. 5e), indicating faster SOR kinetics. The excellent  $V_{Pd}$ -Pd<sub>4</sub>S MNRs activity and smaller Tafel slope are mainly due to the rich vacancies structure which can facilitate the adsorption of reactants/intermediates. The electrolytes after the chronoamperometric (*i*-*t*) curves at different voltages were collected to elucidate the intermediates in the SOR process (Fig. S10). The intensity of the peak signal at 300–370 nm was clearly observed to increase with voltage by ultraviolet–visible (UV–vis) absorbance spectroscopy, suggesting the formation of short chains of polysulfide compounds by successive binding of sulfur ions in the electrolyte (S<sub>2</sub><sup>2−</sup>–S<sub>4</sub><sup>2−</sup>) (Fig. 5f). The  $V_{Pd}$ -Pd<sub>4</sub>S MNRs is a Pd-based sulfide which can promote the formation and further growth of polysulfides, thus effectively avoiding precipitated sulfur from covering the active site to maintain excellent SOR performance [13]. Besides, the electrochemical active area (ECSA) of the sample is one of the powerful evidence to elucidate the high activity, which is assessed by the electrochemical double-layer capacitance (*C*<sub>dl</sub>) obtained through cycle voltammetry (CV) curves (Fig. S11). The calculated *C*<sub>dl</sub> value of the  $V_{Pd}$ -Pd<sub>4</sub>S MNRs is 2.89 mF cm<sup>−2</sup>, which is higher than that of PdMoO<sub>x</sub>

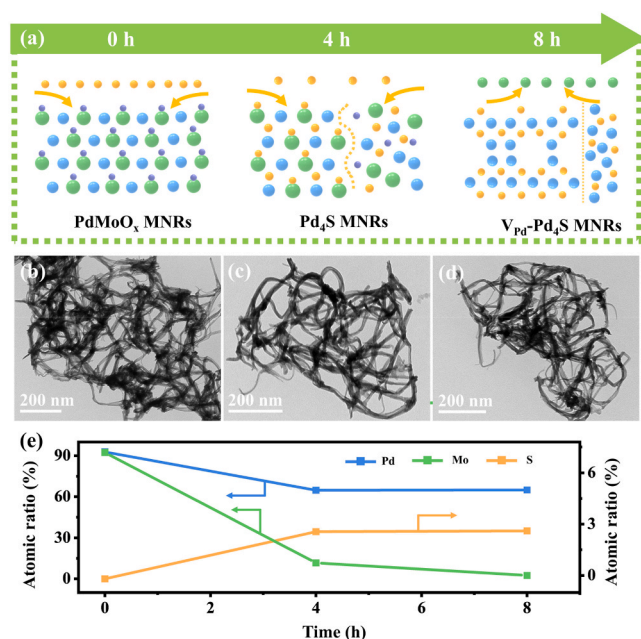
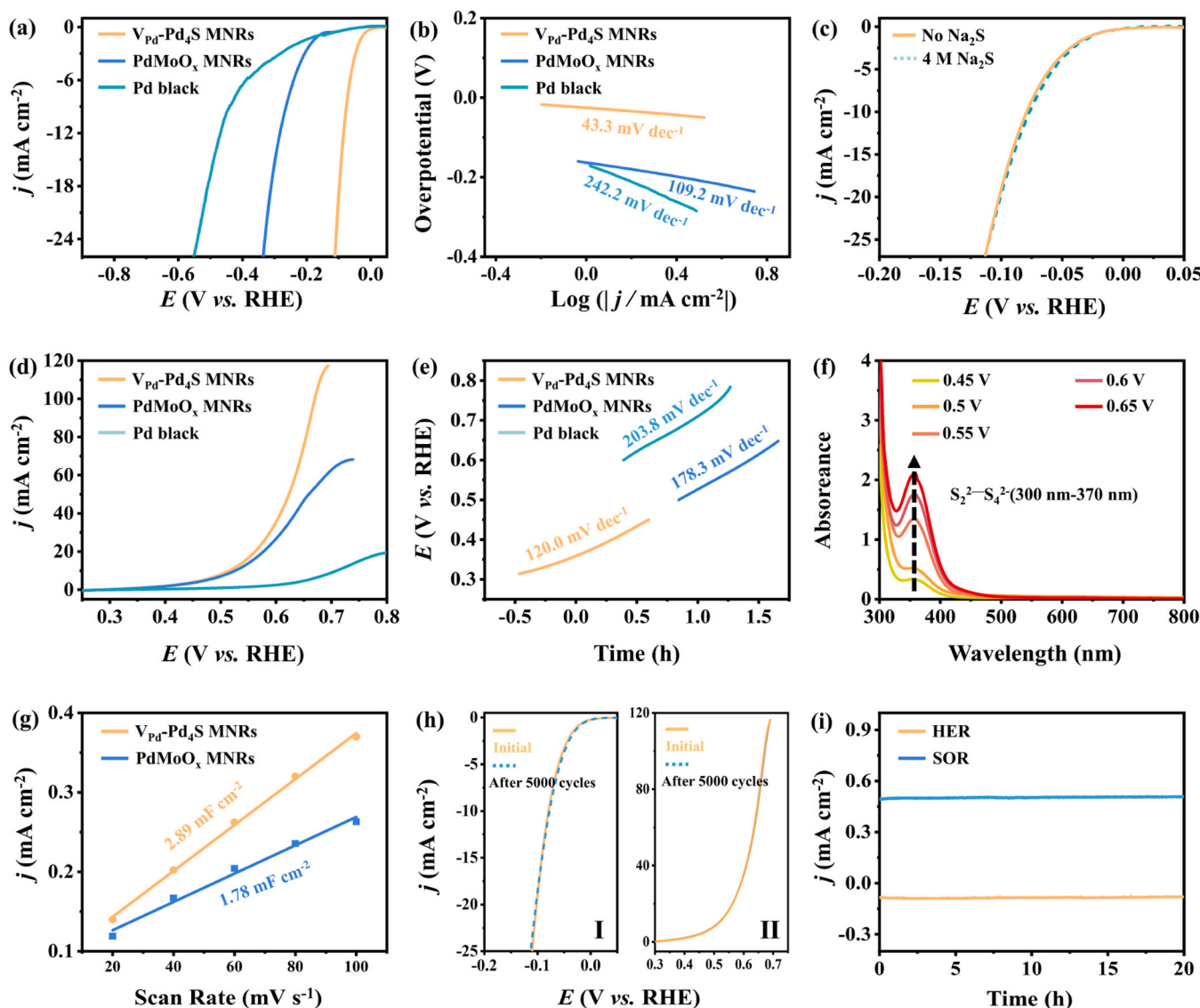


Fig. 4. (a) Schematic diagram of the sulfuration process for PdMoO<sub>x</sub> MNRs. TEM images of  $V_{Pd}$ -Pd<sub>4</sub>S MNRs intermediates obtained after with sulfuration time for (b) 0 h, (c) 4 h and (d) 8 h. (e) Atomic ratios of Pd, Mo and S at different reaction time.



**Fig. 5.** (a) LSV curves and (b) Tafel plots for  $V_{Pd}$ - $Pd_4S$  MNRs,  $PdMoO_x$  MNRs and  $Pd$  black in 1 M KOH. (c) LSV curves for the  $V_{Pd}$ - $Pd_4S$  MNRs in 1 M KOH and 1 M KOH + 4 M  $Na_2S$ . (d) LSV curves for  $V_{Pd}$ - $Pd_4S$  MNRs,  $PdMoO_x$  MNRs and  $Pd$  black 1 M KOH + 4 M  $Na_2S$ . (e) Tafel plots for the various samples. (f) UV-vis spectra of electrolyte at different potentials. (g)  $C_{dl}$  plots for  $V_{Pd}$ - $Pd_4S$  MNRs,  $PdMoO_x$  MNRs. (h) HER (I) and SOR (II) polarization curves for the  $V_{Pd}$ - $Pd_4S$  MNRs before and after 5000 cycles in 1 M KOH solution and 1 M KOH + 4 M  $Na_2S$  solution, respectively. (i) Chronopotentiometry curves for the  $V_{Pd}$ - $Pd_4S$  MNRs at a constant cathodic and anodic current density of  $10\text{ mA cm}^{-2}$  for 20 h.

MNRs ( $1.78\text{ mF cm}^{-2}$ ), directly indicating that the ECSA of  $PdMoO_x$  MNRs increased after sulfuration treatment (Fig. 5g). Except to the catalyst activity, its long-term stability and durability are also the key to achieve remarkable HER and SOR performance. Fig. 5h displays the LSV curves of the  $V_{Pd}$ - $Pd_4S$  MNRs before and after CV tests in 1 M KOH and 1 M KOH + 4 M  $Na_2S$  solutions, respectively. It can be noticed that the LSV is almost the same after 5000 cycles of CV test, which shows the excellent stability of  $V_{Pd}$ - $Pd_4S$  MNRs. Moreover, the chronopotentiometry (v-t) measurements reveal the excellent durability both HER and SOR, and it did not show any significant performance degradation at 20 h (Fig. 5i). The above test results indicate that  $V_{Pd}$ - $Pd_4S$  MNRs has good catalytic performance in both HER and SOR.

### 3.4. HER+SOR coupling system electroactivity of $V_{Pd}$ - $Pd_4S$ MNRs

According to the HER and SOR performance of  $V_{Pd}$ - $Pd_4S$  MNRs at the standard three-electrode described above, the voltage difference between HER, SOR and OER can be calculated. The potential difference

between SOR and HER ( $\Delta V_{S-H} = E_{SOR} - E_{HER} = 0.59\text{ V}$ ) is much lower than the potential difference between OER and HER ( $\Delta V_{O-H} = E_{OER} - E_{HER} = 1.63\text{ V}$ ) (Fig. 6a). The significant reduction in potential difference will undoubtedly contribute to the energy efficiency of  $H_2$  production. Therefore, we constructed a SOR-coupled HER two-electrode system to achieve the dual effect of low-energy  $H_2$  production and simultaneous degradation of sulfur ions. The system employs 1 M KOH as the cathode electrolyte, 1 M KOH + 4 M  $Na_2S$  as the anode electrolyte, and the  $V_{Pd}$ - $Pd_4S$  MNRs/CP simultaneously as the cathode and anode catalysts. As plotted in Fig. 6b, the required applied voltage for the  $V_{Pd}$ - $Pd_4S$  MNRs in the HER+SOR coupled system is significantly lower than that in the OWS system. In particular, Fig. 6c displays the input required voltages to achieve different current densities in the HER+SOR system and the OWS system, respectively. It is clearly observed that the HER+SOR system requires only 0.776 and 0.865 V to provide 100 and  $200\text{ mA cm}^{-2}$  current density much lower than the OWS (2.503 V, 2.626 V).  $V_{Pd}$ - $Pd_4S$  MNRs similarly performs better than most of the other recently reported electrocatalysts in the HER+SOR

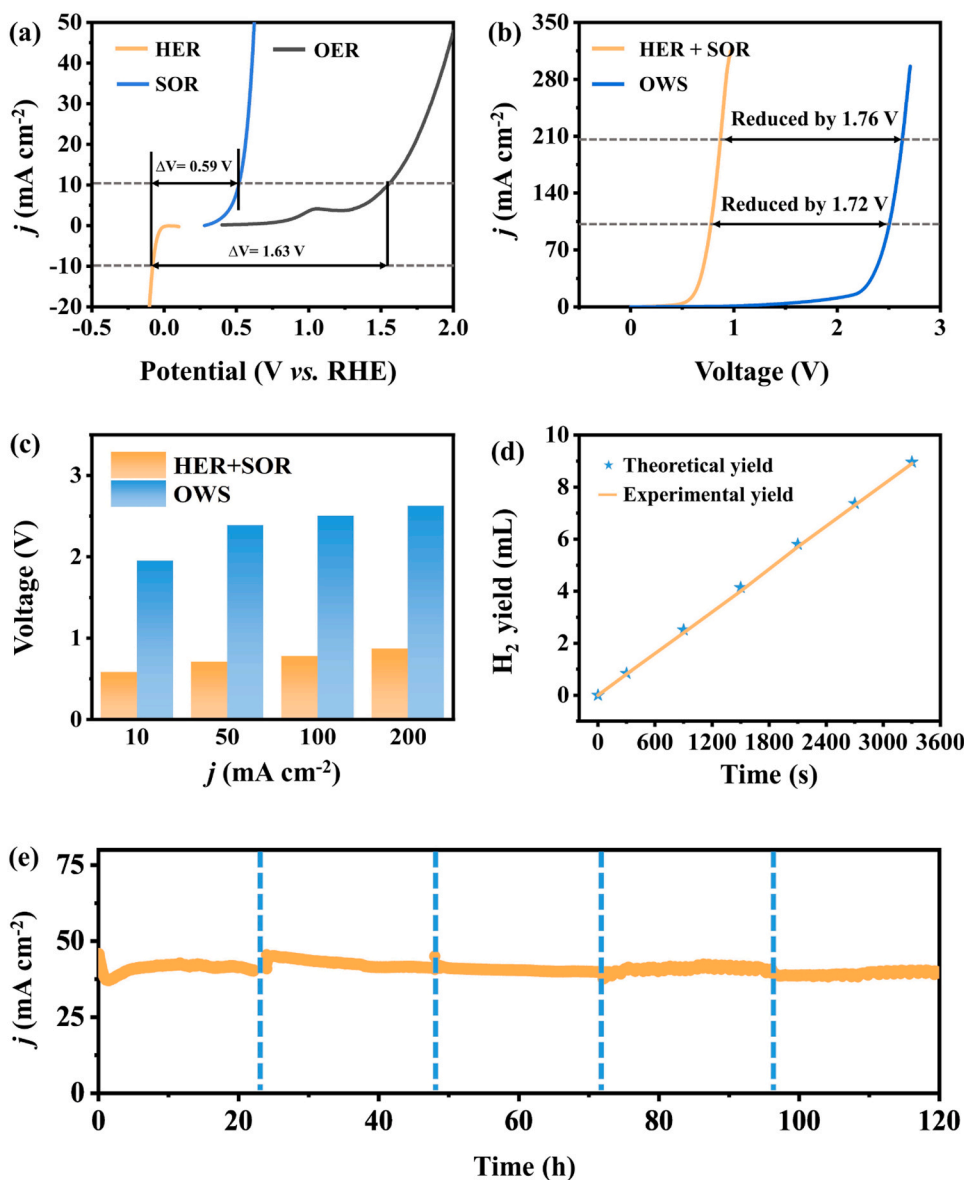


**Fig. 6.** (a) The voltage differences ( $\Delta V$ ) between HER and SOR or OER on  $V_{Pd}$ -Pd<sub>4</sub>S MNRs in different electrolytes. (b) A comparison of the LSVs of HER+SOR and HER+OER in potential. (c) Comparison of the overpotentials required to reach different current densities for HER+SOR and HER+OER. (d) Theoretical and experimental values of H<sub>2</sub> quantity at the cathode during electrolysis. (e) Durability measurement of  $V_{Pd}$ -Pd<sub>4</sub>S MNRs for two-electrode system at 0.5 V for 120 h (the replacement of anodic solution every 24 h).

two-electrode system (Table S2). In order to examine the cathode and anode reaction products, i-t measurement was performed at 0.5 V. The abundant bubble production corresponding to H<sub>2</sub> on the surface of the cathode electrode can be clearly observed (Fig. S12). Meanwhile, the Faraday efficiency (FE) of H<sub>2</sub> production was measured and showed FE close to 100% (Fig. 6d), proving that HER+SOR system is an efficient H<sub>2</sub> production system. In addition, during electrolysis, the anode electrolyte gradually changed from colorless to light yellow and then to dark yellow over time, which reflects the continuous generation of polysulfide compounds (Fig. S13). The anode product was obtained by acidification of the anode electrolyte and tested for XRD, which confirmed that it was sulfur powder (Fig. S14). Furthermore, the stability of the HER+SOR system was tested. It is clear that the current density is stable at the beginning, but decreases with the consumption of Na<sub>2</sub>S at the anode. Therefore, after replacing the anode electrolyte with a fresh one every 24 h, the system current density returned to normal values without significant decay within 120 h, indicating the desirable stability of the  $V_{Pd}$ -Pd<sub>4</sub>S MNRs electrode for HER+SOR system. After long-term stability testing, TEM images show that the morphology of  $V_{Pd}$ -Pd<sub>4</sub>S MNRs still maintains a good nanoribbons structure without significant degradation (Fig. S15). The anode products were collected by every 24 h and

calculated the Faraday efficiency of S production close to 100%, which show that the system is able to efficiently degrade sulfur ions (Fig. S16).

The introduction of vacancies and the crystal-phase plays significant roles for  $V_{Pd}$ -Pd<sub>4</sub>S MNRs with superior HER and SOR properties. Firstly, due to the successful introduction of the S atom, both of the amorphous region and the tetragonal Pd<sub>4</sub>S were formed, simultaneously. The changed of crystal-phase modulate the electron distribution around the Pd atom and led to the appearance of the *d*-band center of Pd near the Fermi energy level, optimizing the adsorption/desorption in the electrocatalytic process. Secondly, Pd vacancies are formed through the deletion of Mo atoms to redistribute the local electrons, and the presence of vacancies can adjust the surface electronic structure of the electrocatalyst, thus accelerating the adsorption of intermediates in the HER/SOR process. Thirdly, the metallene structure and stacked nanoribbons architecture of the  $V_{Pd}$ -Pd<sub>4</sub>S MNRs confers abundant active sites and sufficient channels for mass transfer, respectively.

#### 4. Conclusion

In summary, we have developed an ultrathin Pd<sub>4</sub>S MNRs with Pd-rich vacancies, where vacancy and unconventional crystal-phase were



simultaneously obtained by the process of sulfuration. The  $V_{\text{Pd-Pd}_4\text{S}}$  MNRs display excellent intrinsic activity towards HER and SOR, including both high activity and robust stability. In the SOR-coupled HER system, the  $V_{\text{Pd-Pd}_4\text{S}}$  MNRs requires 0.776 and 0.865 V to reach 100 and 200  $\text{mA cm}^{-2}$ , which is much better than the OWS system (2.503 V, 2.626 V). The outstanding performance of  $V_{\text{Pd-Pd}_4\text{S}}$  MNRs is attributed to unique metallene morphology, Pd vacancies and the crystal-phase. Furthermore, DFT results reveal that the presence of Pd vacancies and electron transfer between Pd and S atoms can modulate the electronic structure and charge distribution on the Pd surface, further optimizing the electronic states near the *d*-band center. This study provides a prospective approach for the rational design and preparation of metallene with vacancy and various crystal-phase for the development of energy-saving  $\text{H}_2$  production systems.

## CRediT authorship contribution statement

**Wenxin Wang:** Experimental measurements, Writing, Investigation, Formal analysis. **Qiqi Mao:** Writing – review & editing, Supervision. **Shaojian Jiang:** Visualization, Data curation. **Kai Deng:** Visualization, Data curation. **Hongjie Yu:** Visualization, Funding acquisition. **Ziqiang Wang:** Writing – review & editing, Supervision, Formal analysis, Funding acquisition. **You Xu:** Writing – review & editing. **Liang Wang:** Conceptualization, Supervision, Visualization, Funding acquisition. **Hongjing Wang:** Supervision, Funding acquisition.

## Declaration of Competing Interest

The authors declare that they have no known competing financial interests or personal relationships that could have appeared to influence the work reported in this paper.

## Data Availability

Data will be made available on request.

## Acknowledgement

This work was financially supported by the National Natural Science Foundation of China (Nos. 21972126, 21978264, 21905250, and 22278369), Natural Science Foundation of Zhejiang Province (No. LQ22B030012 and LQ23B030010), and China Postdoctoral Science Foundation (2021M702889).

## Appendix A. Supporting information

Supplementary data associated with this article can be found in the online version at [doi:10.1016/j.apcatb.2023.123194](https://doi.org/10.1016/j.apcatb.2023.123194).

## References

- [1] D. Liu, A. Barbar, T. Najam, M.S. Javed, J. Shen, P. Tsiakaras, X. Cai, Single noble metal atoms doped 2D materials for catalysis, *Appl. Catal. B: Environ.* 297 (2021), 120389, <https://doi.org/10.1016/j.apcatb.2021.120389>.
- [2] Y. Zeng, M. Zhao, Z. Huang, W. Zhu, J. Zheng, Q. Jiang, Z. Wang, H. Liang, Surface reconstruction of water splitting electrocatalysts, *Adv. Energy Mater.* 12 (2022) 2201713, <https://doi.org/10.1002/aenm.202201713>.
- [3] Z.P. Ifkovits, J.M. Evans, M.C. Meier, K.M. Papadantonakis, N.S. Lewis, Decoupled electrochemical water-splitting systems: a review and perspective, *Energy Environ. Sci.* 14 (2021) 4740–4759, <https://doi.org/10.1039/d1ee01226f>.
- [4] J. Fan, Z. Feng, Y. Mu, X. Ge, D. Wang, L. Zhang, X. Zhao, W. Zhang, D.J. Singh, J. Ma, L. Zheng, W. Zheng, X. Cui, Spatially confined  $\text{PdH}_x$  metallenes by tensile strained atomic Ru layers for efficient hydrogen evolution, *J. Am. Chem. Soc.* 145 (2023) 5710–5717, <https://doi.org/10.1021/jacs.2c11692>.
- [5] C. Cheng, W. Ao, H. Ren, Z. Shen, Z. Fan, T. Xu, W. Liu, Q. Zhang, P. Yin, L. Dai, Heterostructured CNT-RuS<sub>x</sub> nanomaterials for efficient electrochemical hydrogen evolution reaction, *Appl. Catal. B: Environ.* 331 (2023), 122681, <https://doi.org/10.1016/j.apcatb.2023.122681>.
- [6] Z. Pu, T. Liu, G. Zhang, Z. Chen, D.S. Li, N. Chen, W. Chen, Z. Chen, S. Sun, General synthesis of transition-metal-based carbon-group intermetallic catalysts for efficient electrocatalytic hydrogen evolution in wide pH range, *Adv. Energy Mater.* 12 (2022) 2200293, <https://doi.org/10.1002/aenm.202200293>.
- [7] B. Ren, H. Cui, C. Wang, Self-supported graphene nanosheet-based composites as binder-free electrodes for advanced electrochemical energy conversion and storage, *Electrochem. Energy Rev.* 5 (2022) 32, <https://doi.org/10.1007/s41918-022-00138-6>.
- [8] X. Hou, T. Jiang, X. Xu, X. Wang, J. Zhou, H. Xie, Z. Liu, L. Chu, M. Huang, Coupling of NiFe-based metal-organic framework nanosheet arrays with embedded Fe-Ni<sub>3</sub>S<sub>2</sub> clusters as efficient bifunctional electrocatalysts for overall water splitting, *Chin. J. Struct. Chem.* 41 (2022) 2207074–2207080, <https://doi.org/10.14102/j.cnki.0254-5861.2022-0145>.
- [9] Y. Zhang, J. Wu, B. Guo, H. Huo, S. Niu, S. Li, P. Xu, Recent advances of transition-metal metaphosphates for efficient electrocatalytic water splitting, *Carbon Energy* (2023), e375, <https://doi.org/10.1002/cey2.375>.
- [10] Z. Wang, P. Wang, H. Zhang, K. Deng, H. Yu, Y. Xu, X. Li, H. Wang, L. Wang, Energy-efficient hydrogen production coupled with simultaneous electrosynthesis of acetate over a mesoporous OsRh film, *J. Mater. Chem. A* 11 (2023) 8922–8928, <https://doi.org/10.1039/d2ta09621h>.
- [11] F. Chang, M. Xiao, R. Miao, Y. Liu, M. Ren, Z. Jia, D. Han, Y. Yuan, Z. Bai, L. Yang, Copper-based catalysts for electrochemical carbon dioxide reduction to multicarbon products, *Electrochem. Energy Rev.* 5 (2022) 4, <https://doi.org/10.1007/s41918-022-00139-5>.
- [12] W. Huang, T. Bo, S. Zuo, Y. Wang, J. Chen, S. Ould-Chikh, Y. Li, W. Zhou, J. Zhang, H. Zhang, Surface decorated Ni sites for superior photocatalytic hydrogen production, *SusMat* 2 (2022) 466–475, <https://doi.org/10.1002/sus2.76>.
- [13] X. Long, J. Meng, J. Gu, L. Ling, Q. Li, N. Liu, K. Wang, Z. Li, Interfacial engineering of NiFeP/NiFe-LDH heterojunction for efficient overall water splitting, *Chin. J. Struct. Chem.* 41 (2022) 2204046–2204053, <https://doi.org/10.14102/j.cnki.0254-5861.2022-0048>.
- [14] Y. Guo, X. Yang, X. Liu, X. Tong, N. Yang, Coupling methanol oxidation with hydrogen evolution on bifunctional Co-doped Rh electrocatalyst for efficient hydrogen generation, *Adv. Funct. Mater.* 33 (2022) 2209134, <https://doi.org/10.1002/adfm.202209134>.
- [15] E. Gloria, S. Li, A. Mazheika, R. Naumann d'Alnoncourt, A. Thomas, F. Rosowski, CuNi nanoalloys with tunable composition and oxygen defects for the enhancement of the oxygen evolution reaction, *Angew. Chem. Int. Ed.* (2023), e202217888, <https://doi.org/10.1002/anie.202217888>.
- [16] L. Zhang, Z. Wang, J. Qiu, Energy-saving hydrogen production by seawater electrolysis coupling sulfon degradation, *Adv. Mater.* 34 (2022) 2109321, <https://doi.org/10.1002/adma.202109321>.
- [17] L. Yi, Y. Ji, P. Shao, J. Chen, J. Li, H. Li, K. Chen, X. Peng, Z. Wen, Scalable synthesis of tungsten disulfide nanosheets for alkali-acid electrocatalytic sulfon recycling and  $\text{H}_2$  generation, *Angew. Chem. Int. Ed.* 60 (2021) 21550–21557, <https://doi.org/10.1002/anie.202108992>.
- [18] L. Jin, C. Chen, L. Hu, X. Liu, Y. Ding, J. He, H. Li, N. Li, D. Chen, Q. Xu, J. Lu, Ligand-induced electronic structure and morphology regulation in Ni<sub>3</sub>S<sub>2</sub> heterostructures for efficient bifunctional electrocatalysis, *Appl. Surf. Sci.* 605 (2022), 154756, <https://doi.org/10.1016/j.apsusc.2022.154756>.
- [19] Q. Mao, X. Mu, K. Deng, H. Yu, Z. Wang, Y. Xu, X. Li, L. Wang, H. Wang, Sulfur vacancy-rich amorphous Rh metallene sulfide for electrocatalytic selective synthesis of aniline coupled with efficient sulfon degradation, *ACS Nano* 17 (2023) 790–800, <https://doi.org/10.1021/acsnano.2c11094>.
- [20] T. Gao, X. Tang, X. Li, H. Lan, S. Yu, S. Wu, Q. Yue, D. Xiao, Surface reconstructing hierarchical structures as robust sulfon oxidation catalysts to produce hydrogen with ultralow energy consumption, *Inorg. Chem. Front.* 10 (2023) 1447–1456, <https://doi.org/10.1039/d2qi02629e>.
- [21] W. Wang, Q. Mao, K. Deng, H. Yu, Z. Wang, Y. Xu, X. Li, L. Wang, H. Wang, Sulfur-induced low crystallization of ultrathin Pd nanosheet arrays for sulfur ion degradation-assisted energy-efficient  $\text{H}_2$  production, *Small* 19 (2023) 2207852, <https://doi.org/10.1002/smll.202207852>.
- [22] H. Wang, W. Wang, H. Yu, Q. Mao, Y. Xu, X. Li, Z. Wang, L. Wang, Interface engineering of polyaniline-functionalized porous Pd metallene for alkaline oxygen reduction reaction, *Appl. Catal. B: Environ.* 307 (2022), 121172, <https://doi.org/10.1016/j.apcatb.2022.121172>.
- [23] X. Yang, J.H. Lee, S. Kattel, B. Xu, J.G. Chen, Tuning reaction pathways of electrochemical conversion of  $\text{CO}_2$  by growing Pd shells on Ag nanocubes, *Nano Lett.* 22 (2022) 4576–4582, <https://doi.org/10.1021/acs.nanolett.2c01667>.
- [24] Y. Li, P. Kidkhunthod, Y. Zhou, X. Wang, J.M. Lee, Dense heterointerfaces and unsaturated coordination synergistically accelerate electrocatalysis in Pt/Pt<sub>5</sub>P<sub>2</sub> porous nanocages, *Adv. Funct. Mater.* 32 (2022) 2205985, <https://doi.org/10.1002/adfm.202205985>.
- [25] H. Cheng, N. Yang, G. Liu, Y. Ge, J. Huang, Q. Yun, Y. Du, C.J. Sun, B. Chen, J. Liu, H. Zhang, Ligand-exchange-induced amorphization of Pd nanomaterials for highly efficient electrocatalytic hydrogen evolution reaction, *Adv. Mater.* 32 (2020), e1902964, <https://doi.org/10.1002/adma.201902964>.
- [26] Z. Wang, S. Xu, M. Li, K. Deng, H. Yu, Y. Xu, X. Li, H. Wang, L. Wang, Polyethyleneimine-functionalized PdOs bimetallics for enhanced oxygen reduction, *Chem. Commun.* 59 (2023) 4511–4514, <https://doi.org/10.1039/d3cc00221g>.
- [27] J. Wu, J. Fan, X. Zhao, Y. Wang, D. Wang, H. Liu, L. Gu, Q. Zhang, L. Zheng, D. J. Singh, X. Cui, W. Zheng, Atomically dispersed MoO<sub>x</sub> on rhodium metallene boosts electrocatalyzed alkaline hydrogen evolution, *Angew. Chem. Int. Ed.* 61 (2022), e202207512, <https://doi.org/10.1002/anie.202207512>.
- [28] Q. Mao, W. Wang, K. Deng, H. Yu, Z. Wang, Y. Xu, X. Li, L. Wang, H. Wang, Low-content Pt-triggered the optimized d-band center of Rh metallene for energy-saving

- hydrogen production coupled with hydrazine degradation, *J. Energy Chem.* 85 (2023) 58–66, <https://doi.org/10.1016/j.jechem.2023.06.005>.
- [29] Q. Mao, X. Mu, K. Deng, H. Yu, Z. Wang, Y. Xu, X. Li, L. Wang, H. Wang, Multisite synergism-induced electron regulation of high-entropy alloy metallene for boosting alkaline hydrogen evolution reaction, *Adv. Funct. Mater.* (2023) 2304963, <https://doi.org/10.1002/adfm.202304963>.
- [30] Y. Kang, Y. Tang, L. Zhu, B. Jiang, X. Xu, O. Guselnikova, H. Li, T. Asahi, Y. Yamauchi, Porous nanoarchitectures of nonprecious metal borides: From controlled synthesis to heterogeneous catalyst applications, *ACS Catal.* 12 (2022) 14773–14793, <https://doi.org/10.1021/acscatal.2c03480>.
- [31] Y. Kang, M.K. Masud, Y. Guo, Y. Zhao, Z.S. Nishat, J. Zhao, B. Jiang, Y. Sugahara, T. Pejovic, T. Morgan, M.S.A. Hossain, H. Li, C. Salomon, T. Asahi, Y. Yamauchi, Au-loaded superparamagnetic mesoporous bimetallic CoFeB nanovehicles for sensitive autoantibody detection, *ACS Nano* 17 (2023) 3346–3357, <https://doi.org/10.1021/acsnano.2c07694>.
- [32] S. Liu, H. Zhang, H. Yu, K. Deng, Z. Wang, Y. Xu, L. Wang, H. Wang, Tailored design of PdRh bimetallic nanoribbons by solvent-induced strategy for efficient alkaline hydrogen evolution, *Appl. Catal. B: Environ.* 336 (2023), 122948, <https://doi.org/10.1039/d0cs01079k>.
- [33] W. Li, D. Wang, Y. Zhang, L. Tao, T. Wang, Y. Zou, Y. Wang, R. Chen, S. Wang, Defect engineering for fuel-cell electrocatalysts, *Adv. Mater.* 32 (2020) 1907879, <https://doi.org/10.1002/adma.201907879>.
- [34] X. Yang, Y. Wang, X. Tong, N. Yang, Strain engineering in electrocatalysts: fundamentals, progress, and perspectives, *Adv. Energy Mater.* 12 (2021) 2102261, <https://doi.org/10.1002/aenm.202102261>.
- [35] W. Song, M. Li, C. Wang, X. Lu, Electronic modulation and interface engineering of electropump nanomaterials-based electrocatalysts toward water splitting, *Carbon Energy* 3 (2020) 101–128, <https://doi.org/10.1002/cey2.85>.
- [36] Z. Wu, Y. Zhao, W. Jin, B. Jia, J. Wang, T. Ma, Recent Progress of vacancy engineering for electrochemical energy conversion related applications, *Adv. Funct. Mater.* 31 (2020) 2009070, <https://doi.org/10.1002/adfm.202009070>.
- [37] X. Wang, J. Wu, Y. Zhang, Y. Sun, K. Ma, Y. Xie, W. Zheng, Z. Tian, Z. Kang, Y. Zhang, Vacancy defects in 2D transition metal dichalcogenide electrocatalysts: From aggregated to atomic configuration, *Adv. Mater.* (2022), e2206576, <https://doi.org/10.1002/adma.202206576>.
- [38] Z. Wang, H. Zhao, J. Liu, D. Zhang, X. Wu, N. Nie, D. Wu, W. Xu, J. Lai, L. Wang, The PdH<sub>x</sub> metallene with vacancies for synergistically enhancing electrocatalytic N<sub>2</sub> fixation, *Chem. Eng. J.* 450 (2022), 137951, <https://doi.org/10.1016/j.cej.2022.137951>.
- [39] F. Lin, F. Lv, Q. Zhang, H. Luo, K. Wang, J. Zhou, W. Zhang, W. Zhang, D. Wang, L. Gu, S. Guo, Local coordination regulation through tuning atomic-scale cavities of Pd metallene toward efficient oxygen reduction electrocatalysis, *Adv. Mater.* 34 (2022) 2202084, <https://doi.org/10.1002/adma.202202084>.
- [40] D. Yan, C. Xia, W. Zhang, Q. Hu, C. He, B.Y. Xia, S. Wang, Cation defect engineering of transition metal electrocatalysts for oxygen evolution reaction, *Adv. Energy Mater.* 12 (2022) 2202317, <https://doi.org/10.1002/aenm.202202317>.
- [41] L. Zhai, T.W. Benedict Lo, Z.-L. Xu, J. Potter, J. Mo, X. Guo, C.C. Tang, S.C. Edman Tsang, S.P. Lau, In situ phase transformation on nickel-based selenides for enhanced hydrogen evolution reaction in alkaline medium, *ACS Energy Lett.* 5 (2020) 2483–2491, <https://doi.org/10.1021/acsenenergylett.0c01385>.
- [42] Y. Chen, Z. Lai, X. Zhang, Z. Fan, Q. He, C. Tan, H. Zhang, Phase engineering of nanomaterials, *Nat. Rev. Chem.* 4 (2020) 243–256, <https://doi.org/10.1038/s41570-020-0173-4>.
- [43] L. Chen, L.-R. Zhang, L.-Y. Yao, Y.-H. Fang, L. He, G.-F. Wei, Z.-P. Liu, Metal boride better than Pt: HCP Pd<sub>2</sub>B as a superactive hydrogen evolution reaction catalyst, *Energy Environ. Sci.* 12 (2019) 3099–3105, <https://doi.org/10.1039/c9ee01564g>.
- [44] Y. Xu, K. Ren, T. Ren, M. Wang, S. Yu, Z. Wang, X. Li, L. Wang, H. Wang, Phosphorus-triggered modification of the electronic structure and surface properties of Pd<sub>4</sub>S nanowires for robust hydrogen evolution electrocatalysis, *J. Mater. Chem. A* 8 (2020) 19873–19878, <https://doi.org/10.1039/d0ta07403a>.
- [45] L. Jin, R. Ji, H. Wan, J. He, P. Gu, H. Lin, Q. Xu, J. Lu, Boosting the electrocatalytic urea oxidation performance by amorphous–crystalline Ni-TPA@NiSe heterostructures and mechanism discovery, *ACS Catal.* 13 (2022) 837–847, <https://doi.org/10.1021/acscatal.2c05546>.
- [46] L. Zhang, H. Jang, H. Liu, M.G. Kim, D. Yang, S. Liu, X. Liu, J. Cho, Sodium-decorated amorphous/crystalline RuO<sub>2</sub> with rich oxygen vacancies: a robust pH-universal oxygen evolution electrocatalyst, *Angew. Chem. Int. Ed.* 60 (2021) 18821–18829, <https://doi.org/10.1002/anie.202106631>.
- [47] B. Jiang, H. Xue, P. Wang, H. Du, Y. Kang, J. Zhao, S. Wang, W. Zhou, Z. Bian, H. Li, J. Henzie, Y. Yamauchi, Noble-metal-metalloid alloy architectures: Mesoporous amorphous Iridium–Tellurium alloy for electrochemical N<sub>2</sub> reduction, *J. Am. Chem. Soc.* 145 (2023) 6079–6086, <https://doi.org/10.1021/jacs.2c10637>.
- [48] Y. Kang, J. Henzie, H. Gu, J. Na, A. Fatehmulla, B.S.A. Shamsan, A.M. Aldhafiri, W. A. Farooq, Y. Bando, T. Asahi, B. Jiang, H. Li, Y. Yamauchi, Mesoporous metal-metalloid amorphous alloys: The first synthesis of open 3D mesoporous Ni-B amorphous alloy spheres via a dual chemical reduction method, *Small* 16 (2020) 1906707, <https://doi.org/10.1002/smll.201906707>.
- [49] S. Shen, Z. Wang, Z. Lin, K. Song, Q. Zhang, F. Meng, L. Gu, W. Zhong, Crystalline-amorphous interfaces coupling of CoSe<sub>2</sub>/CoP with optimized d-band center and boosted electrocatalytic hydrogen evolution, *Adv. Mater.* 34 (2022) 2110631, <https://doi.org/10.1002/adma.202110631>.
- [50] Q. Gao, W. Luo, X. Ma, Z. Ma, S. Li, F. Gou, W. Shen, Y. Jiang, R. He, M. Li, Electronic modulation and vacancy engineering of Ni<sub>9</sub>S<sub>8</sub> to synergistically boost efficient water splitting: Active vacancy-metal pairs, *Appl. Catal. B: Environ.* 310 (2022), 121356, <https://doi.org/10.1016/j.apcatb.2022.121356>.
- [51] S. Liu, H. Zhang, H. Yu, K. Deng, Z. Wang, Y. Xu, L. Wang, H. Wang, Defect-rich PdIr bimetallic nanoribbons with interatomic charge localization for isopropanol-assisted seawater splitting, *Small* 19 (2023) 2300388, <https://doi.org/10.1002/smll.202300388>.
- [52] X. Chen, J. Wan, J. Wang, Q. Zhang, L. Gu, L. Zheng, N. Wang, R. Yu, Atomically dispersed ruthenium on nickel hydroxide ultrathin nanoribbons for highly efficient hydrogen evolution reaction in alkaline media, *Adv. Mater.* 33 (2021) 2104764, <https://doi.org/10.1002/adma.202104764>.
- [53] M. Zhu, Q. Shao, Y. Pi, J. Guo, B. Huang, Y. Qian, X. Huang, Ultrathin vein-like iridium-tin nanowires with abundant oxidized tin as high-performance ethanol oxidation electrocatalysts, *Small* 13 (2017) 1701295, <https://doi.org/10.1002/smll.201701295>.
- [54] M. Xie, B. Zhang, Z. Jin, P. Li, G. Yu, Atomically reconstructed palladium metallene by intercalation-induced lattice expansion and amorphization for highly efficient electrocatalysis, *ACS Nano* 16 (2022) 13715–13727, <https://doi.org/10.1021/acsnano.2c05190>.
- [55] Q. Huang, F. Dang, H. Zhu, L. Zhao, B. He, Y. Wang, J. Wang, X. Mai, A hierarchical porous carbon supported Pd@Pd<sub>4</sub>S heterostructure as an efficient catalytic material positive electrode for Li–O<sub>2</sub> batteries, *J. Power Sources* 451 (2020), 227738, <https://doi.org/10.1016/j.jpowsour.2020.227738>.
- [56] L. Su, Y. Zhao, Y. Jin, Z. Liu, H. Cui, W. Luo, Identifying the role of hydroxyl binding energy in a non-monotonous behavior of Pd-Pd<sub>4</sub>S for hydrogen oxidation reaction, *Adv. Funct. Mater.* 32 (2022) 2113047, <https://doi.org/10.1002/adfm.202113047>.
- [57] G. Zhang, A. Wang, L. Niu, W. Gao, W. Hu, Z. Liu, R. Wang, J. Chen, Interfacial engineering to construct antioxidant Pd<sub>4</sub>S/Pd<sub>3</sub>P<sub>0.95</sub> heterostructure for robust hydrogen production at high current density, *Adv. Energy Mater.* 12 (2022) 2103511, <https://doi.org/10.1002/aenm.202103511>.
- [58] Z. Li, M. Huang, J. Li, H. Zhu, Large-scale, controllable synthesis of ultrathin platinum diselenide ribbons for efficient electrocatalytic hydrogen evolution, *Adv. Funct. Mater.* 33 (2023) 2300376, <https://doi.org/10.1002/adfm.202300376>.
- [59] X. Kang, Z. Jin, H. Peng, Z. Cheng, L. Liu, X. Li, X. Xie, J. Zhang, Y. Dong, The role of selenium vacancies functionalized mediator of bimetal (Co, Fe) selenide for high-energy-density lithium-sulfur batteries, *J. Colloid Interface Sci.* 637 (2023) 161–172, <https://doi.org/10.1016/j.jcis.2023.01.090>.
- [60] H. Xin, Z. Dai, Y. Zhao, S. Guo, J. Sun, Q. Luo, P. Zhang, L. Sun, N. Ogiwara, H. Kitagawa, B. Huang, F. Ma, Recording the Pt-beyond hydrogen production electrocatalysis by dirhodium phosphide with an overpotential of only 4.3 mV in alkaline electrolyte, *Appl. Catal. B: Environ.* 297 (2021), 120457, <https://doi.org/10.1016/j.apcatb.2021.120457>.
- [61] M. Tosun, L. Chan, M. Amani, T. Roy, G.H. Ahn, P. Taheri, C. Carraro, J.W. Ager, R. Maboudian, A. Javey, Air-stable n-doping of WSe<sub>2</sub> by anion vacancy formation with mild plasma treatment, *ACS Nano* 10 (2016) 6853–6860, <https://doi.org/10.1021/acsnano.6b02521>.
- [62] Y. Liu, A.J. McCue, J. Feng, S. Guan, D. Li, J.A. Anderson, Evolution of palladium sulfide phases during thermal treatments and consequences for acetylene hydrogenation, *J. Catal.* 364 (2018) 204–215, <https://doi.org/10.1016/j.jcat.2018.05.018>.
- [63] Y. Wu, Y. Zhao, M. Zhou, S. Tan, R. Peymanfar, B. Aslibeiki, G. Ji, Ultrabroad microwave absorption ability and infrared stealth property of nano-micro CuS@rGO lightweight aerogels, *Nano-Micro Lett.* 14 (2022) 171, <https://doi.org/10.1007/s40820-022-00906-5>.
- [64] L. Zhuang, L. Ge, Y. Yang, M. Li, Y. Jia, X. Yao, Z. Zhu, Ultrathin iron-cobalt oxide nanosheets with abundant oxygen vacancies for the oxygen evolution reaction, *Adv. Mater.* 29 (2017) 1606793, <https://doi.org/10.1002/adma.201606793>.
- [65] X. Yu, Z.-Y. Yu, X.-L. Zhang, P. Li, B. Sun, X. Gao, K. Yan, H. Liu, Y. Duan, M.-R. Gao, G. Wang, S.-H. Yu, Highly disordered cobalt oxide nanostructure induced by sulfur incorporation for efficient overall water splitting, *Nano Energy* 71 (2020), 104652, <https://doi.org/10.1016/j.nanoen.2020.104652>.
- [66] N. Guo, H. Xue, A. Bao, Z. Wang, J. Sun, T. Song, X. Ge, W. Zhang, K. Huang, F. He, Q. Wang, Achieving superior electrocatalytic performance by surface copper vacancy defects during electrochemical etching process, *Angew. Chem. Int. Ed.* 59 (2020) 13778–13784, <https://doi.org/10.1002/anie.202002394>.
- [67] J. Sun, H. Xue, Y. Zhang, X.L. Zhang, N. Guo, T. Song, H. Dong, Y. Kong, J. Zhang, Q. Wang, Unraveling the synergistic effect of heteroatomic substitution and vacancy engineering in CoFe<sub>2</sub>O<sub>4</sub> for superior electrocatalysis performance, *Nano Lett.* 22 (2022) 3503–3511, <https://doi.org/10.1021/acsnanolett.1c04425>.
- [68] X. Cao, Y. Tan, H. Zheng, J. Hu, X. Chen, Z. Chen, Effect of cobalt phosphide (CoP) vacancies on its hydrogen evolution activity via water splitting: a theoretical study, *Phys. Chem. Chem. Phys.* 24 (2022) 4644–4652, <https://doi.org/10.1039/d1cp05739a>.
- [69] Y. Zhao, N. Jia, X.-R. Wu, F.-M. Li, P. Chen, P.-J. Jin, S. Yin, Y. Chen, Rhodium phosphide ultrathin nanosheets for hydrazine oxidation boosted electrochemical water splitting, *Appl. Catal. B: Environ.* 270 (2020), 118880, <https://doi.org/10.1016/j.apcatb.2020.118880>.
- [70] Q. Xue, H. Huang, J.-Y. Zhu, Y. Zhao, F.-M. Li, P. Chen, Y. Chen, Au@Rh core-shell nanowires for hydrazine electrooxidation, *Appl. Catal. B: Environ.* 278 (2020), 119269, <https://doi.org/10.1016/j.apcatb.2020.119269>.
- [71] J. Zhu, L. Hu, P. Zhao, L.Y.S. Lee, K.Y. Wong, Recent advances in electrocatalytic hydrogen evolution using nanoparticles, *Chem. Rev.* 120 (2020) 851–918, <https://doi.org/10.1021/acs.chemrev.9b00248>.